Fe doping induced selenium vacancy on cobalt selenide for enhanced hydrogen peroxides production

Jun Wang [a], Xiaomei Liu [a], Tao Liao [a], Chengbo Ma [a], Bin Chen [a], Yang Li [a,b], Xiaobin Fan [a,b], Wenchao Peng [a,b,*]

[a] *School of Chemical Engineering and Technology, Tianjin University, Tianjin 300350, PR China*
[b] *Institute of Shaoxing, Tianjin University, Zhejiang 312300, PR China*

ARTICLE INFO

ABSTRACT

Electrocatalytic two-electron oxygen reduction reaction (2e-ORR) pathway for hydrogen peroxides (H_2O_2) generation has emerges as an appealing alternative to conventional anthraquinone craft. In this work, Fe doped CoSe was synthesized via hydrothermal and subsequent high temperature (HT) annealing process. The doping of trace amount of Fe could tune the crystal growth direction and induce the generation of Se vacancy during annealing. During the Electrocatalytic measurement, the Faraday efficiency of 2e-ORR can reach 99.1%, 83.2% and 93.6% in 0.1 M KOH, 0.1 M Na_2SO_4, and 0.05 M H_2SO_4, respectively. Under the neutral condition, the production rate of H_2O_2 reached 18.37 mmol L^{-1} in 120 min. Moreover, Fe-CoSe-HT exhibits good stability and Fe^{2+} regeneration during flow-Fenton reaction. Hence, the dual role of selenium-vacancy-enriched Fe-CoSe-HT greatly enhanced selectivity of 2e-ORR and accelerated Fe reduction, resulting in promoted •OH radical generation and organic pollutants treatment.

1. Introduction

As a fundamental and ecofriendly oxidant, hydrogen peroxide (H_2O_2) is widely applied in medical industries and chemical synthesis, as well as in decolorization craft and wastewater treatment [1,2]. Currently, the high-energy consumption anthraquinone method is the mainstream technology for high concentration H_2O_2 production, along with environmental deterioration and transport risks [3,4]. Therefore, developing an efficient and sustainable generation strategy is crucial for the broad H_2O_2 requirement [5]. Based on the energy transition and carbon neutrality background, electrocatalytic two electron oxygen reduction (2e-ORR) is considered as the potential alternative strategy for H_2O_2 generation, which can achieve low energy consumption and on-demand scale [6]. However, oxygen (O_2) in cathode can simultaneously generate H_2O by-product through the four electron (4e-ORR) oxygen reduction reaction, resulting in the sharp decrease of H_2O_2 yield. [7,8]. To this end, seeking a highly conversion efficiency and selectivity 2e-ORR electrocatalyst is a core challenge for oxygen reduction.

Theoretically, O_2 molecules will be chemically adsorbed on the surface of active site and form *OOH intermediate via side-on (*O–OH*) or end-on (*OOH*) configurations during the initial activation stage [9].

Usually, the side-on adsorption model in *OOH intermediate tends to form adsorbed oxygen (*O) through the crack of "O-O" bond in *OOH, which is then converted into H_2O through the four electron (4e-ORR) pathway [10,11]. For end-on (*OOH*) adsorption, the adsorbed "*OOH" species can directly escape from catalyst surface and form the target H_2O_2 product through one step electron transfer [12–14]. Therefore, the adsorption configuration and corresponding intensity are crucial for the further conversion of *OOH intermediates. Some noble metal alloys, including Pd-Au, Ag–Hg and Au–Pt electrodes could adsorb *OOH strongly and achieve efficient H_2O_2 formation. The application is however limited by their rare and expensive. Most of the pristine carbon allotropes (graphene, CNT, fullerene, etc.) and transition metals (Fe, Mn, Ni, Cu, etc.) tend to undergo the 4e-ORR [15–17]. Introducing functionalized oxygen functional groups (C=O and C-O-C) and edge defects (armchairs and zigzag) configurations onto these carbon allotropes could improve their performance in 2e-ORR process, current density value and stability of these carbons still need to be increased [18, 19]. Up to now, many other strategies are also investigated to achieve the conversion of two electron to four electron pathway, such as heteroatom doping [20], defect project [21,22], vacancy engineer [23,24], heterostructure [25], size regulation [26], spatial coordination [27,28],

---

* Corresponding author at: School of Chemical Engineering and Technology, Tianjin University, Tianjin 300350, PR China.
  E-mail address: wenchao.peng@tju.edu.cn (W. Peng).

crystal plane [29] and so on. Despite numerous tactics has been attempted, unsatisfactory selectivity as well as poor stability greatly restricted the application of electrocatalytic for H_2O_2 production in energy devices [30].

Compared to chemically similar oxygen or sulfur elements, selenium (Se) doped two-phase or polymetallic heterostructures have recently been shown to have high oxygen reduction performance, which is probably because its metalloid specific and tolerance [31,32]. As a semiconductor element with a direct bandgap, Se element also has a flexible valence state and is prone to induce carrier migration and create adequate vacancy during the crystal transition process [33]. The selenium vacancy at a specific position on catalyst could ameliorate the electron cloud distribution, promoting the heterolysis of adsorbed *OOH intermediate, regulating the effectively conversion of oxygen reduction process from 4e-ORR to 2e-ORR pathway [23,34].

Considering the electronic characteristics of selenide and the mechanism of oxygen reduction, we innovatively synthesized the selenium-vacancy-enriched Fe-CoSe-HT catalyst through facile hydrothermal and subsequent high temperature (HT) annealing and applied it for electrocatalysis 2e-ORR process. For structure identification, XPS spectroscopy, EPR analysis and DFT calculation can be used to confirm the rich selenium vacancy in Fe-CoSe-HT. The performance of electrocatalytic 2e-ORR was tested on rotating ring disk (RRDE) electrode. Apart from evaluating Faraday efficiency and electron transfer numbers, we also evaluated the actual capacity of Fe-CoSe-HT for H_2O_2 in H-cell and gas diffusion (GDE) electrode to prove the key role of Se vacancies. Moreover, Fe-CoSe-HT exhibits good stability and Fe^{2+} regeneration in the flow-Fenton system. 100% RhB removal efficiency with outstanding stability is achieved in 12 h. Hence, the dual role of selenium-vacancy-enriched Fe-CoSe-HT provides a new insight into the coupling technique of electrocatalytic H_2O_2 generation and organic pollutants treatment.

2. Experiments

2.1. Chemicals

The cobalt acetate tetrahydrate (Co $(AC)_2 \cdot 4\ H_2O$, 99%), diethylenetriamine (DETA, 99%), sodium selenite pentahydrate ($Na_2SeO_3 \cdot 5\ H_2O$, 99%), iron dichloride tetrahydrate ($FeCl_2.4\ H_2O$, 99%), hydrochloric acid (HCl, 37%), sodium sulphate (Na_2SO_4, 99%), sodium sulphate (KOH, 99%), hydrogen peroxide solution (H_2O_2, 30 wt%), sulfuric acid (H_2SO_4, 98%) and nafion solution (5 wt%)) were obtained from Sigma-Aldrich. Rhodamine B (Rh B), cerium (IV) sulfate (Ce $(SO_4)_2$, 98%), isopropanol (IPA, 99%) and absolute ethanol were bought from Macklin. All reagents for material synthesis and electrocatalysis 2e-ORR were conducted without purification.

2.2. Synthesis of Fe-CoSe-HT

In this work, selenium-vacancy-enriched sample was prepared via hydrothermal and further annealing treatment. Briefly, 0.537 g Co $(AC)_2 \cdot 4\ H_2O$ and 0.536 g $Na_2SeO_3 \cdot 5\ H_2O$ were dissolved into 36 ml H_2O and stirred 0.5 h to form a clear aqueous solution. 0.083 g $FeCl_2.4\ H_2O$ and 36 ml DETA was then separately added with 1 h continuous intermix. Subsequently, the obtained mixed solution was heated in 100 ml polytetrafluoroethylene kettle at 180 °C for 12 h. By washing with water and ethanol and further centrifugation, the solid precursor (denoted as Fe-CoSe) was then heated at 60 °C for 12 h. For annealing stage, Fe-CoSe sample was transferred to the corundum boat and annealed at 400 °C for 0.5 h at a ramping rate of 10 °C min^{-1} under an argon (200 sccm) atmosphere. After high temperature annealing (abbreviated as HT process) and three times water washing, the final Fe-CoSe-HT material was obtained. The synthesis approach of CoSe and CoSe-HT were similar to CoSe and Fe-CoSe, respectively, only without the addition of $FeCl_2.4\ H_2O$ source precursor.

2.3. Characterization

The composition and existence form of nother species in Fe-CoSe-HT was determined by XRD (Bruker, smartlab) and Raman spectroscopy (Thermo Fischer DXR). The morphological information was examined with HR-SEM (Hitachi, S4800) and AC HAADF-STEM (JEOL JEM-ARM200F). Specific surface areas (SSAs) as well as relevant pore size distribution were characterized by Bjbuilder SSA-7000. The existing forms and valence states of elements was identified through X-ray photoelectron spectroscope (Thermo ESCALAB 250XI). Vibration signals generated by structural defects was recorded on Raman spectra (Thermo Fischer DXR) using 532 nm laser as the excitation source. Contact angle and surface tension was measured by contact angle measuring device (Biolin, theta Flow). For catalytic efficiency test, the concentration of residual RhB was conducted by HPLC (Thermo, UltiMate 3000). The existence of Se-vacancy (100 K) and reactive oxidation species (ROSs) were analyzed by EPR spectra (Bruker EMXplus).

2.4. Electrochemical measurements

Electrocatalytic 2e-ORR were implemented by typical three-electrode electrochemical measurement in which graphite rod as well as Ag electrode with assured potential (0.197 V) is selected as counter electrode and reference electrode, respectively. The generated H_2O_2 on disk electrode is rapidly captured by Pt ring electrode and further reduced to H_2O at the voltage of 1.2 V, generating a current electrical signal. Experimental calibration of RRDE collection efficiency was conducted in ring electrode through the redox of $K_3Fe(CN)_6$. The polarization curve of linear sweep voltammetry (LSV) is measured by rotating disk electrode at a speed of 1600 rpm. The deducted background current is obtained under the same conditions in saturated N_2 atmosphere. The selectivity of electrocatalysis 2e-ORR process for H_2O_2 product is calculated by the following formula:

$$H_2O_2\,selectivity(\%) = 200 \times \frac{\left(\frac{I_r}{N_c}\right)}{\left(|I_d| + \frac{I_r}{N_c}\right)} \tag{1}$$

$$n = 4 \times \frac{|I_d|}{\left(|I_d| + \frac{I_r}{N_c}\right)} \tag{2}$$

where I_r, I_d and N_c represent the ring current, disk current and H_2O_2 collection efficiency, respectively.

2.5. DFT Calculations

Density functional theory is calculated by VASP program with PAW measure through first principles. During the iteration, all atomic positions are completely slack until the force is less than 0.02 eV Å^{-1} under the cut-off energy of 500 eV and demanding precision (10^{-4} eV). The PBE gradient and van der Waals (vdW) interaction have been applied in the approximate (GGA) exchange and DFT-D3 methods, respectively. For specific model construction, the slab model of CoSe (101), CoSe -V (Se) (101), Fe-CoSe (101) and Fe-CoSe-HT (101) surfaces were constructed from the optimized crystal structure. We set different spacings in the c-axis direction to represent the different interlayer spacings of the catalyst. For an ideal catalyst for electroreduction of ORR, the catalyst not only will provide high activity through minimizing the overpotential for the 2e-ORR pathway to H_2O_2, but also possess high selectivity by suppressing the 4e-ORR to H_2O. Computational hydrogen electrode (CHE) model used to determine the Gibbs energy change (ΔE_{ads}) of intermediates:

$$\Delta G_{ads} = \Delta E_{ads} + \Delta ZPE - T\Delta S + eU \tag{3}$$

where E_{ads}, ZPE, S, e and U represent the adsorption energy, zero-point

energy, entropy, transfer electron and applied voltage, respectively.

3. Results and discussion

3.1. Synthesis and characterization of Fe-CoSe-HT material

The selenium-vacancy-enriched Fe-CoSe-HT catalyst was synthesized through hydrothermal and further annealing (Fig. 1a). For hydrothermal stage, $Co(AC)_2 \cdot 4 H_2O$ and $Na_2SeO_3 \cdot 5 H_2O$ were served as Co and Se source separately to form CoSe. Simultaneously, trace amount of $FeCl_2 \cdot 4 H_2O$ was added to the precursor for to generate FeSe. For the second pyrolysis stage (400 °C), the harsh condition causes the transformation of FeSe to Fe_3Se_4 species, resulting in the loss of Se and generation of Se vacancy in Fe-CoSe-HT material.

In order to clarify the specific structure, XRD pattern test was firstly implemented (Fig. 1b). The apparent peaks at 33.2°, 44.7°, 50.5° and 60.3° belong to the (101), (102), (110) and (103) lattice of $Co_{0.85}Se$ species (PDF#52–1008), respectively [35]. Due to the close peak

position and small amout of $FeCl_2 \cdot 4 H_2O$, the signal of Fe species is difficult to distinguish in the XRD spectra of Fe-CoSe-HT [36,37]. However, obvious peak at 33.9°, 45.6°, 51.6° and 63.2° of FeSe (PDF#75–0608) appeared in Fe-CoSe with the increased addition amount of $FeCl_2 \cdot 4 H_2O$ (Fig. S1) [38]. Furthermore, Fe species were transformed from FeSe to Fe_3Se_4 (PDF#73–2021) during the second annealing stage [39]. Attributing to the increasing demand of Se/Fe ratio in Fe_3Se_4, inadequate Se will therefore lead to the generation of Se vacancy in the near Fe-Se-Co site. In addition, the proportion of crystal plane in CoSe, CoSe-HT, Fe-CoSe and Fe-CoSe-HT were investigated. The texture coefficient (TC) for all facets of CoSe species are calculated using Haris formula ($TC_{(hkl)} = (I_i/I_0)/(\frac{1}{n}\sum_{i=1}^{n}\frac{I_i}{I_0})$), where I_i and I_0 are the XRD intensity of standard powder and investigated samples, respectively [40]. As shown in Fig. 1c, the TC value of the CoSe (101) facet shows an increasing trend, indicating that the addition of Fe species and further annealing can accelerate the preferential growth of CoSe (101). As shown in Fig. 1d, the specific surface area (SSA) of CoSe, CoSe-HT and Fe-CoSe and Fe-CoSe-HT are 27.04, 38.51, 52.51 and 86.87 m^2
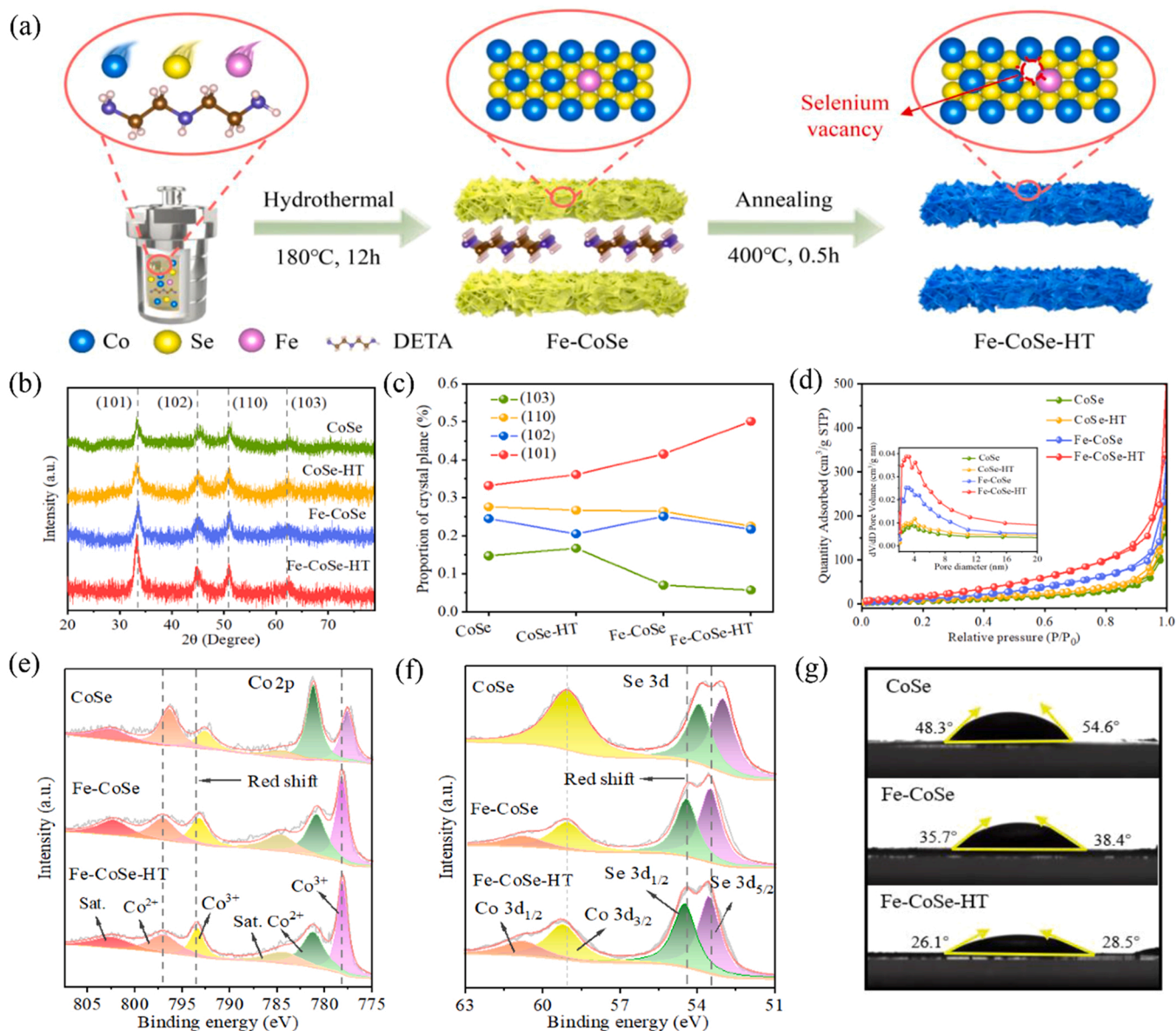

Fig. 1. (a) Synthetic illustration of selenium-vacancy-enriched Fe-CoSe-HT monolayers via hydrothermal and further annealing treatment, (b) XRD patterns and (c) corresponding crystal plane proportion, (d) N_2 adsorption-desorption isotherms curves (inset of d was the related pore size distribution), (e) Co 2p XPS, (f) Se 3d XPS survey and (g) digital photos showing the contact angles of CoSe, Fe-CoSe and Fe-CoSe-HT materials, respectively.

g^{-1}, along with the average pore diameter at 17.95 nm (Table S1). As a layered and two-dimensional material, the increase of (101) crystal plane and SSA in Fe-CoSe-HT will promote the exposure of potential active sites.

The chemical composition of Fe-CoSe-HT were characterized by XPS (Table S2). Fig. 1e displays the Co 2p XPS spectra of CoSe, Fe CoSe and Fe-CoSe-HT samples, respectively. Compared with CoSe (777.86 eV), remarkable positive shift (+0.70 eV) could be observed in Fe CoSe and Fe-CoSe-HT, which can be attributed to the decrease Co coordination by Se abscond [41]. Meanwhile, two peaks corresponding to Se $3d_{5/2}$ and Se $3d_{1/2}$ at 52.79 and 53.62 eV in CoSe shifted to 53.35 and 54.14 eV for Fe-CoSe and Fe-CoSe-HT samples, respectively (Fig. 1f) [42]. The obvious shift of Se 3d peak should be ascribed to the rich selenium vacancy. Besides, the other peak pair at 58.60 and 60.06 eV for Fe-CoSe-HT corresponds to Co^{3+} and Co^{2+} species, respectively [43]. Similar to the peak at 777.86 eV, there is an equally non-negligible shift of binding energy at 58.60 eV. The Fe 2p XPS signals at 710.71, 713.14, 715.09 and 718.21 eV can be attributed to Fe^{2+}, Fe^{3+} and satellite peaks (Fig. S2) [44]. Compared with Fe-CoSe, there is a significant increase of Fe^{3+} species (51.3–56.7%) for Fe-CoSe-HT. Hence, increased Se demand during annealing process creates conditions for vacancy generation. For electrocatalysis, the wettability of synthetic materials has a noteworthy effect on improving mass transfer and ion diffusion. Fig. 1g manifests

digital photos of electrolyte wettability by static contact angle measurements [45]. It is evident that Fe-CoSe-HT present smaller average contact angle values (27.30°) than that of CoSe (27.3°) and Fe-CoSe (51.45°), indicating its better hydrophilicity, which would allow the improvement of electrocatalytic activity.

The morphology of synthetic CoSe was detected by scanning electron microscopy (SEM) investigation. As shown in Fig. 2a and Fig. S3a-c, both CoSe and CoSe-HT samples without trace Fe doping exhibit dense nanoribbons structure [46]. Surprisingly, Fe doped CoSe (Fe-CoSe) directly forms interlaced nanosheet array during the first hydrothermal stage (Fig. 2b and Fig. S3d-f). Furthermore, Fe-CoSe-HT maintains the similar morphology structure with Fe-CoSe after annealing process. Theoretically, distinctive selenium coordination numbers (FeSe and $Co_{0.85}Se$) and electronegativity of introduced Fe promotes the rotation of Co-Se and Fe-Se bonds during Fe-CoSe-HT crystal growth process. With the specific substitution of Co by Fe atoms, CoSe monolayer would grow in different directions, resulting in the formation of nanoflakes structure. For electro-catalysis, interlaced nanoflake arrays in Fe-CoSe-HT are conducive to the exposure of active site and the rapid transfer of generated H_2O_2 product. The high-resolution TEM lattice (Fig. 2c) and converted FFT fringes (Fig. 2d) near 2.68 Å both correspond to the (101) crystal plane of Fe-CoSe-HT material, respectively.

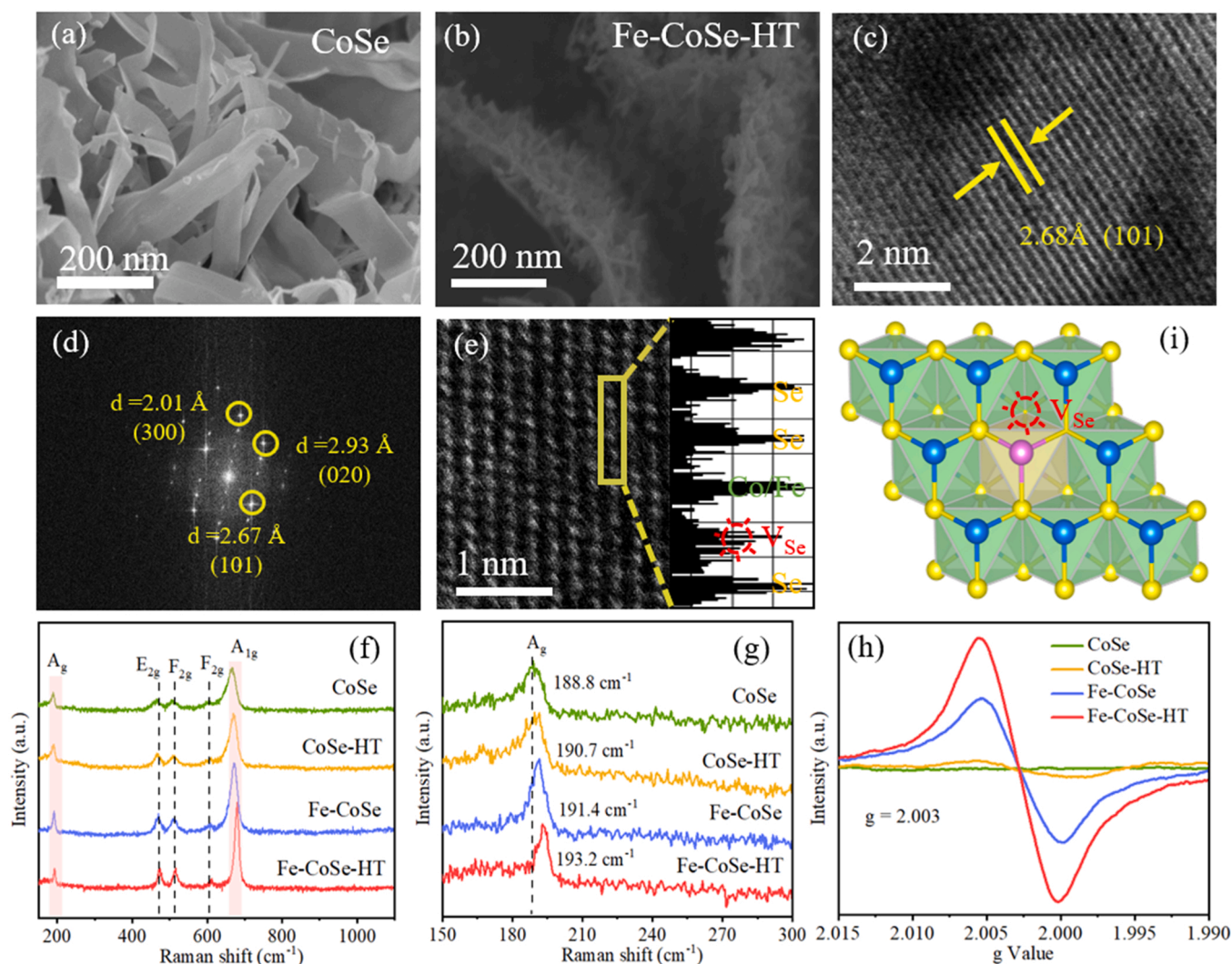Furthermore, the fine atom-configuration comparison of CoSe and

Fig. 2. (a) SEM image of CoSe, (b) SEM image, (c) HR-TEM image and (d) the corresponding inverse FFT images of Fe-CoSe-HT, (e) high-resolution high-angle annular dark-field STEM (HAADF-STEM) image and (f) the computed structure in Fe-CoSe-HT material, (g-h) Raman spectra and (i) EPR spectra (100 K) of CoSe, CoSe-HT, Fe-CoSe and Fe-CoSe-HT materials, respectively.

Fe-CoSe-HT are explored by AC HR-TEM test. As shown in Fig. S3g, Co and Se atoms in CoSe crystal are arranged in an orderly manner. It is worth noting that the introduction of Fe causes a lot of structure defects in Fe-CoSe (Fig. S3h) which creates a prerequisite for the isomerization of crystal form and Se vacancy generation during the second annealing process. The missing Se atoms on the finally obtained Fe-CoSe-HT surface can be observed through the intensity distribution-map (Fig. 2e). Along the periodic arrangement of Co (Fe) and Se atoms direction, there is obvious Se deficiency, indicating the existence of Se vacancy. The HAADF-STEM image and the corresponding mapping analysis (Fig. S3i) demonstrate the uniform distribution of elements (Co, Se and Fe) in Fe-CoSe-HT. According the latest study, the red-shift of Co-Se (A_g and $A_{1\,g}$) bending vibration signal by Raman spectra is an efficient approach to verify structural defects in CoSe material [47]. Compared with CoSe (Fig. 2f-g), the significant offset confirms the Se vacancy in Fe-CoSe-HT structure. Typically, Electron paramagnetic resonance (EPR) spectra is one of the most effective technologies to verify the presence of vacancy [48]. Compared with CoSe and CoSe-HT, there is a upgraded intensity of microtherm EPR (100 K) spectra of Fe-CoSe (Fig. 2h) g = 2.008 value [49]. Followed by annealing at 400 °C, the signal of Se vacancy for obtained Fe-CoSe-HT is greatly enhanced. Altogether, the above results of XPS, HR-TEM, Raman spectra and EPR spectra further authenticate the enriched Se vacancy in synthesized Fe-CoSe-HT material (Fig. 2i).

3.2. Electrocatalytic Oxygen Reduction (2e-ORR) measurement

The 2e-ORR test of the as-prepared catalysts was evaluated on rotating ring disk (RRDE) electrode through three-electrode system [50]. The generated H_2O_2 on disk electrode is rapidly captured by Pt ring electrode and further reduced to H_2O at the voltage of 1.2 V [51]. The linear sweep voltammetry (LSV) curves of the CoSe, CoSe-HT, Fe-CoSe and Fe-CoSe-HT samples in 0.1 M Na_2SO_4 were displayed in Fig. 3a. Specifically, the disk current (bottom) and ring current (upper) are the current responses generated by the total oxygen reduction (ORR) and the two electron (2e-ORR) pathway, respectively. Compared with CoSe, CoSe-HT and Fe-CoSe, Fe-CoSe-HT shows the highest ring current, which suggests that most amount of H_2O_2 generation. The H_2O_2 selectivity of different CoSe samples can be measured by the calculated Faraday efficiency. As shown in Fig. 3b. Fe-CoSe-HT possesses the highest H_2O_2 selectivity, and a striking H_2O_2 selectivity nearly 83.1% is obtained among 0–0.5 V (vs. RHE), indicating the dominant 2e-ORR pathway. Meanwhile, CoSe-HT shows the slightly lower H_2O_2 selectivity, which is around 48.4%. The H_2O_2 selectivity of CoSe-HT and Fe-CoSe displays a remarkable fluctuation (0.2 eV vs. RHE) with the
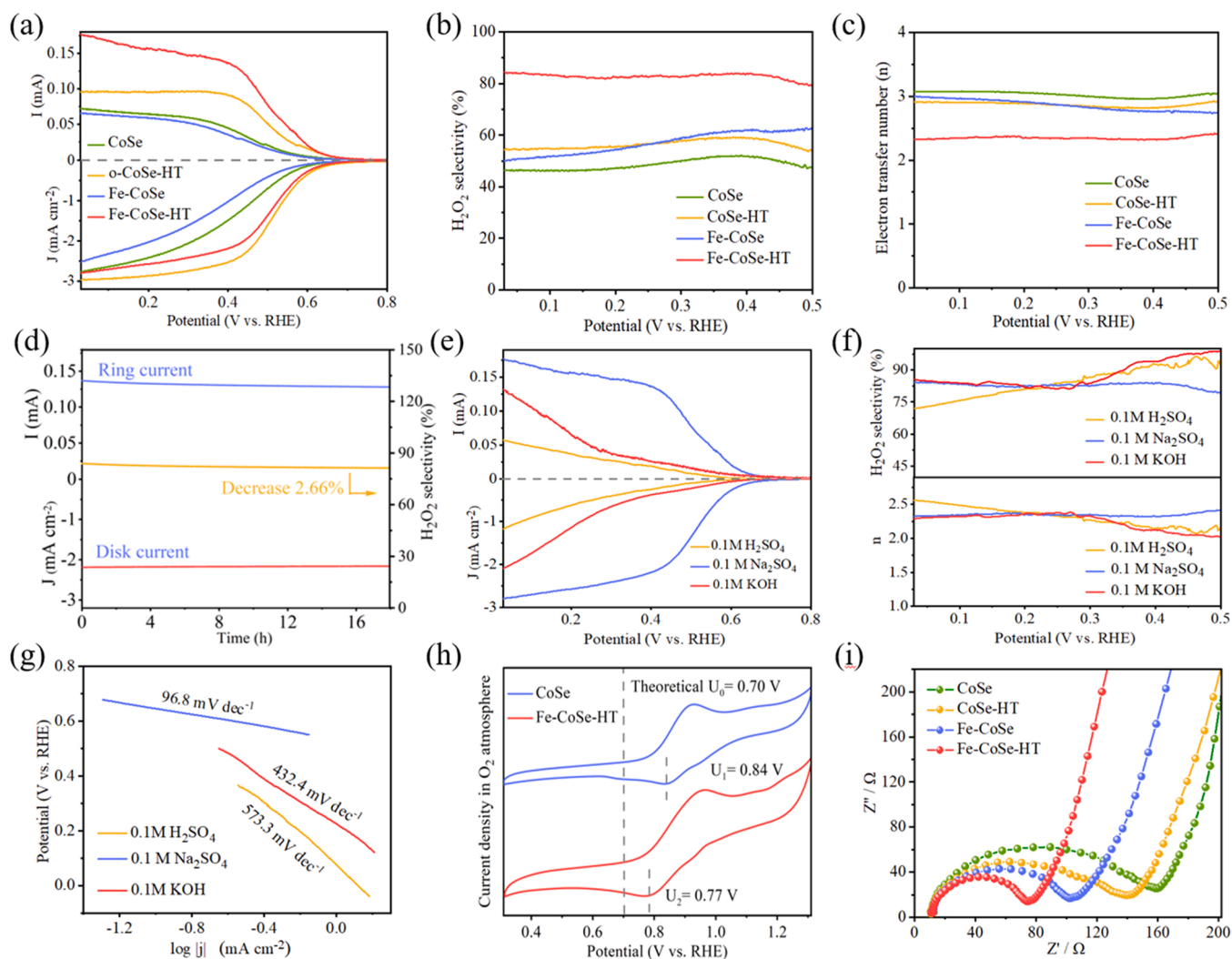

Fig. 3. (a) LSV curves of CoSe, CoSe-HT, Fe-CoSe and Fe-CoSe-HT materials. (b) The calculated Faraday efficiency and (c) electron transfer number of CoSe, CoSe-HT, Fe-CoSe and Fe-CoSe-HT materials. (d) The chronoamperometry curve and corresponding H_2O_2 selectivity of Fe-CoSe-HT in 18 h. (e) the comparison of faradaic efficiency selectivity in various electrolytes under 0.1 M KOH, 0.1 M Na_2SO_4 and 0.05 M H_2SO_4, (f) related H_2O_2 selectivity as well as electron transfer number calculation and (g) Tafel plots. (h) CV curves of the indicated electrodes in N_2 saturated 0.1 M Na_2SO_4 solution and (i) EIS curves.

value between 53.9% and 55.2%. Theoretically, the electron transfer numbers calculated for 2e-ORR and 4e-ORR are 2 and 4, respectively. The calculation results indicate that CoSe-HT, Fe-CoSe and Fe-CoSe-HT samples deliver the electron transfer number of 2.89, 2.94, 3.08 and 2.32, respectively (Fig. 3**c**). The maximum Faraday efficiency and minimum electron selectivity confirm the distinguished 2e-ORR activity of Fe-CoSe-HT among these samples. Notably, the Fe-CoSe-HT also shows superior 2e-ORR performance compared with other state-of-the-art electrocatalysts (Table S3). Besides, the durability test of Fe-CoSe-HT was then employed in 0.1 M Na_2SO_4 by chronoamperometry. As shown in Fig. 3**d**, only about 2.66% selectivity attenuation is observed even after 18 h test, indicating its long-term stability.

Furthermore, the stability of Fe-CoSe-HT catalyst under higher current density is an important factor for industrialization. Hence, the linear scanning voltammetry (LSV) and chronoamperometry (i-t) of Fe-CoSe-HT coated on carbon cloth has been added. High current density was observed with the assistance of carbon cloth, indicating the potential of H_2O_2 production on a large scale (Fig. S4). For 2e-ORR process, the loading capacity of Fe-CoSe-HT plays an important role in H_2O_2 selectivity, which is further optimized (Fig. S5). The selectivity is improved with the increases of loading amount increases from 20 to 60 ug cm^{-2}. However, the Faraday efficiency is gradually decreased with the increase of loading amount (100 ug cm^{-2}), which could be attributed to the reduced mass transfer of generated H_2O_2. In addition, the rotating speed of RRDE electrode from 400 to 1600 rpm was conducted. It is obvious that the rotating speed has negligible influence on H_2O_2 selectivity (Fig. S6a-**c**). According to the fitting of disk and ring current, the collection efficiency is determined as nearly 0.35, closing to the theoretical value measured by $K_3Fe(CN)_6$ reduction process [21].

The H_2O_2 selectivity of Fe-CoSe-HT in different pH surroundings, including 0.1 M KOH, 0.1 M Na_2SO_4 and 0.05 M H_2SO_4 was then explored (Fig. 3**e**). Compared with the 2e-ORR in alkaline and acidic conditions, Fe-CoSe-HT exhibits more attractive limit current and selectivity under neutral conditions. In addition, the H_2O_2 selectivity and electron transfer number of Fe-CoSe-HT in alkaline and acidic conditions are explored. In 0.1 M KOH, nearly 100% H_2O_2 selectivity can be achieved at the initial high voltage (Fig. 3**f**). However, the current density and selectivity significantly decreased with increasing voltage, ultimately maintaining a Faraday efficiency of 85.3% at 0.1 V (vs.RHE). Besides, dramatical attenuation also exists in acidic (0.05 M H_2SO_4) environments. Despite owning high selectivity (93.6%) at 0.5 V (vs. RHE), H_2O_2 selectivity is rapidly reduced to 73.08% with the increase of voltage to 0.1 V. The greatly reduced selectivity can be attributed to the poor stability of Fe-CoSe-HT under strong acid condition. Correspondingly, the Tafel plots of Fe-CoSe-HT in alkaline, neutral and acidic conditions are 432.4, 96.8 and 573.3 mV dec^{-1}, respectively (Fig. 3**g**). Similarly, CoSe, CoSe-HT and Fe-CoSe under neutral also present the highest ring current density, as well as the remarkable attenuation of Faradaic efficiency in acidic conditions (Fig. S7). Hence, it could be seen that neutral environment is the most effective condition for H_2O_2 generation when using Fe-CoSe-HT as electrode.

The ORR catalytic activities are further evaluated by voltammetry (CV) curves acquired in N_2-saturated 0.1 M Na_2SO_4 in wide scope (0–1.6 V vs. RHE). Theoretically, the redox peaks of Co^{2+}/Co^{3+} and Co^{3+}/Co^{4+} in N_2-saturated system for Co-based material usually appear at 1.2 and 1.44 V, respectively (Fig. S8) [52]. However, only double layer charging profile exist during the charging and discharging process. The non-existent redox peak of Fe-CoSe-HT implies the electrochemical stability of Fe-CoSe-HT during 2e-ORR electrocatalysis. The thermodynamic oxidation reduction potential of O_2 to H_2O_2 is 0.7 V (vs.RHE). As shown in Fig. 3**h**, the 2e-ORR potential of CoSe and Fe-CoSe-HT under O_2-saturated 0.1 M Na_2SO_4 solution are 0.77 and 0.84 eV, confirming the enhanced electrocatalytic activity of Fe-CoSe-HT (Fig. 3**i**) [53]. Electrochemical impedance spectroscopy (EIS) spectroscopy can directly analyze the electron transfer ability of Fe-CoSe-HT catalyst

during 2e-ORR process. The fitting charge transfer resistance (R_{ct}) in Nyquist plots of CoSe, CoSe-HT, Fe-CoSe and Fe-CoSe-HT are 90.3, 128.8, 146.9 and 63.4 Ω for annealed Fe-CoSe at 0.236 V overpotential. The minimum R_{ct} of Fe-CoSe-HT greatly promoted charge transfer kinetics on Fe-CoSe-HT catalyst, which is beneficial for the increase of 2e-ORR electrochemical activity [54].

3.3. DFT calculation for electrocatalytic oxygen reduction reaction

The generation of *OOH intermediate and activation pathway comparison in CoSe and Fe-CoSe-HT catalyst during ORR process can be explored by DFT calculation. Fig. 4**a-b** show the detailed structure of four models with Fe doping or Se vacancy and calculated density of state (DOS). It could be seen that Fe-CoSe-V(Se) with Fe induced Se vacancy has the largest density of state (15.12 eV) at Fermi level, indicating the great contribution to the electron transport. For ORR process, O_2 will firstly adsorb on the surface of catalyst to form *OOH intermediate. The results of charge-density difference between *OOH and active indicates that adsorbed *OOH on Fe-CoSe-V(Se) exhibits more apparent electron transfer (Fig. 4**c-d**). Therefore, the Gibbs free energy of *OOH in diverse structural models was calculated. The CoSe, CoSe-V(Se), Fe-CoSe and Fe-CoSe-V(Se) samples deliver free energies of + 0.60, − 0.17, + 0.33 and + 0.04 eV deviation, indicating the competitive *OOH adsorption of Fe-CoSe-V(Se) in side-on bonding (Fig. 4**e**). Apart of that, the Gibbs energy change in potential 2e-ORR and 4e-ORR pathways at 0 eV (vs. RHE) is simulated (Fig. 4**f**). The OOH* intermediates adsorbed on CoSe and Fe-CoSe-V(Se) are + 0.6 eV and − 1.37 eV, respectively. A smaller adsorption energy can greatly promote the oxygen reduction (ORR) process. For *OH reduction and desorption step during 4e-ORR, the energy demand on Fe-CoSe-V(Se) to H_2O is positive (+0.84 eV). A large energy barrier greatly inferior the 4e-ORR pathway, resulting in enhancement of 2e-ORR activity. To compare the ORR activities of these CoSe samples, the free energy diagrams and constructed the activity-volcano plots for 2e-ORR pathway by using ΔG_{*OOH} as a descriptor (Fig. 4**g**). Compared with the pristine CoSe model, the Fe-CoSe-V(Se) has the supreme U_L value (0.61 V) to *OOH intermediate at 4.18 eV, favoring the 2e-ORR rather than 4e-ORR process. Totally, the relevant activation mechanism of 2e-ORR and 4e-ORR on CoSe and Fe-CoSe-V(Se) models are specifically described in Fig. 4**h**. During the activation process, O_2 is firstly adsorbed on the surface of active through electronic transmission to form *OOH intermediate. For 4e-ORR, the O-O bond in *OOH in CoSe would breakup to form *O species. Followed by the conversion of *O to *OH, H_2O would be eventually formed through the four-electron process. However, the adsorbed *OOH in Fe-CoSe-V(Se) will be directly converted into H_2O_2 during 2e-ORR process.

3.4. Combined system of 2e-ORR and flow-Fenton reaction

The measurement of H_2O_2 production capability of synthesized Fe-CoSe-HT catalyst under bulk electrolysis condition was examined in an H-cell separated by an anion exchange membrane with different electrolyte solution. The H_2O_2 productivity was determined via cerium sulfate $Ce(SO_4)_2$ oxidation titration and related calibration curve was showed in Fig. S9. In traditional H-Cell reactor (Fig. 5**a**), the H_2O_2 production rates of 1.36, 2.17, 5.61 mmol L^{-1} are achieved under acidic, alkaline, and neutral conditions respectively at a at a cell output voltage of 0.2 V. Therefore, neutral condition is much more effective for the bulk electrosynthesis of H_2O_2 that can reach practically useful concentrations.

Gas diffusion electrode (GDE) enables efficient synthesis of ORR process with its excellent air diffusion performance, which may provide enhanced efficiency for on-site production of H_2O_2. Here, we compared the H_2O_2 production of GDE electrode with the conventional H-Cell electrode. Different from the traditional two-phase interface transfer of H-Cell system, the gas diffusion layer builds a triple-phase boundary for O_2 diffusion (Fig. 5**b**). Surprisingly, the concentration of H_2O_2 product
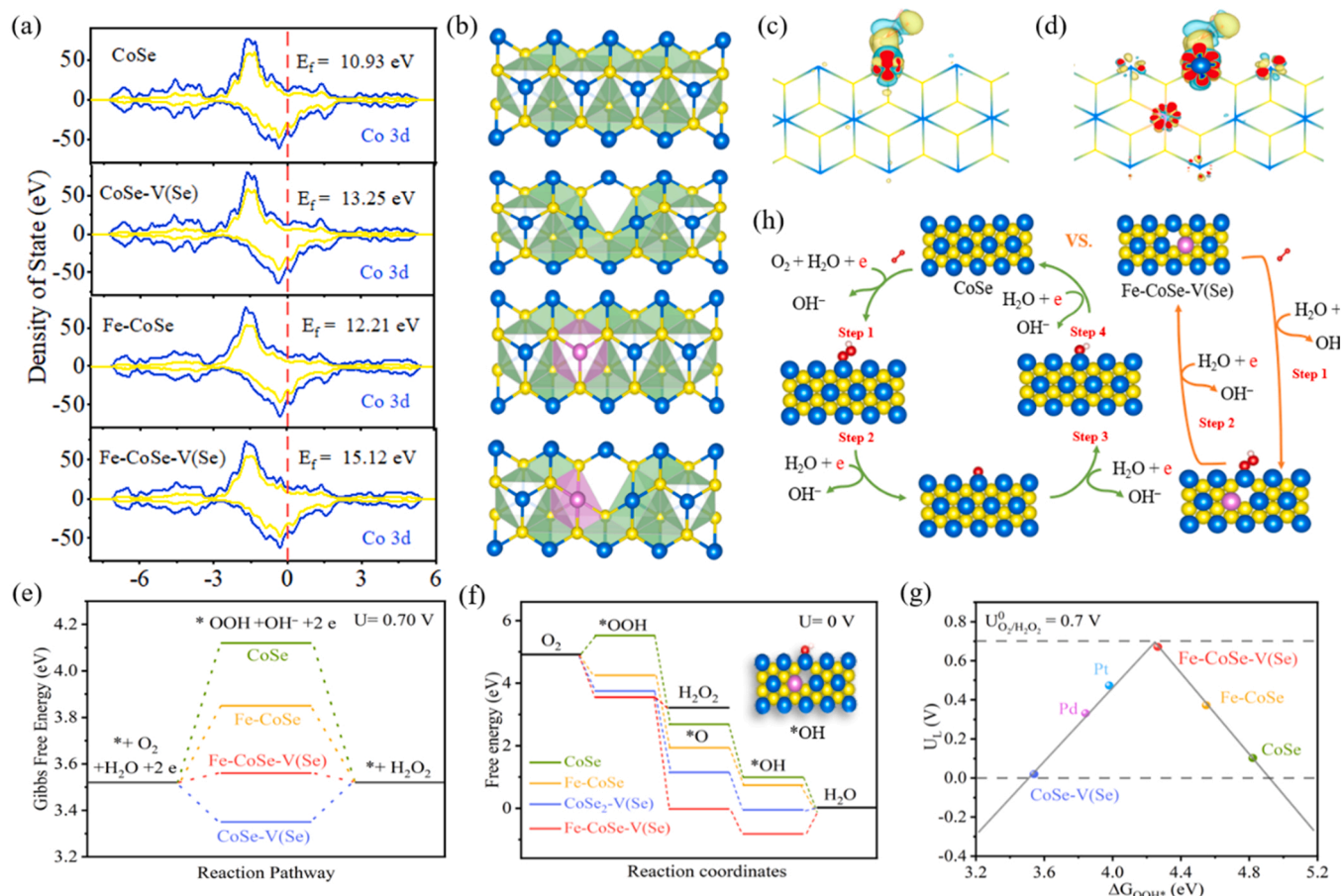
Fig. 4. (a) Density of states (DOS) and (b) four basic structural (CoSe, CoSe-V(Se), Fe-CoSe and Fe-CoSe-V(Se)) models, (c-d) difference Charge-density of *OOH, (e) formation energy of adsorptive *OOH intermediate at 0.7 V, (f) comparison of 2e-ORR and 4e-ORR pathways, (g) 2e-ORR activity volcano plot and (h) contrasting catalytic activation pathways on different models.

reached 18.37 mmol L^{-1} within 120 min for GDE electrode, almost 3.27 times than H-Cell system (Fig. 5c). Hence, the optimization of mass transfer is equally important for 2e-ORR. As the most practical technologies in wastewater treatments, Fenton reactions can effectively remove organic contaminants by producing active species (ROS) or non-radical processes. Among various ROS, hydroxyl radicals ($^{\bullet}OH$) generated by Fenton reagent (Fe^{2+}/H_2O_2) has a miraculous effect to trace pollutants removal because of its powerful oxidant potential (2.80 V). In this work, H_2O_2 generated in GDE electrode was delivered to a flow tubular reactor device to trigger the degradation process (Fig. 5d).

For wastewater treatment, the pH of Fe^{2+} and Rhodamine B (Rh B) mixture was adjusted to 2.8–3.0 for an optimal activation environment. Then, H_2O_2 and pollutants are delivered to the electrode chamber through peristaltic pump. Without Fe^{2+} species (Fig. 5e), less than 10.64% Rh B removal efficiency is achieved, indicating the poor H_2O_2 activation ability of Fe-CoSe-HT. With the addition of Fe^{2+}, the removal efficiency of Rh B increased to 70.24%. However, almost 100% Rh B could be removed when Fe-CoSe-HT is packed in the column device. During H_2O_2 activation, Fe^{2+} is easily converted to Fe^{3+} (40–80 M^{-1} S^{-1}), while the reduction of Fe^{3+} to Fe^{2+} is not complete because of the weak reaction rate (9.1×10^{-7} M^{-1} S^{-1}). In order to determine the role of Fe-CoSe-HT, Fe^{3+} and Fe^{2+} concentrations are investigated by phenanthroline method through UV–vis–NIR spectrometer. The ratio of Fe^{2+}/Fe^{3+} species was only 15.6% while the reduction efficiency reached 37.54% in Fe-CoSe-HT/ Fe^{2+}/H_2O_2 system (Fig. 5f). Hence, the addition of Fe-CoSe-HT is conducive to the excellent electron-donor characteristic and Fe^{2+} regeneration during the degradation process. Typically, quenchers can interact with specific reactive oxidation

species (Table S3). As shown in Fig. 5g, the catalytic activity of Fe-CoSe-HT is slightly inhibited with the addition of furfuryl alcohol (FFA), β-carotene and L-histidine and benzoquinone (BQ) even at a high concentration, indicating the weak contribution of $^1O_2$ for RhB degradation. When benzoquinone (BQ) is added in the degradation system, there is a similar weak quenching result. Hence, $O_2^{\bullet-}$ radical is not the dominant active species, either. Whereas, remarkable reduction is occurred by the quenching of tert-butanol (TBA) and methanol (MeOH), confirming the key role of $\bullet$ OH radical (Fig. S10). The existence of $^{\bullet}OH$ radical could be detected by electron paramagnetic resonance (EPR) spectroscopy (Fig. 5h). Besides, the peak intensity of DMPO-OOH is significantly increased when Fe-CoSe-HT is introduced, indicating the accelerated Fe reduction. Combined with the electro-catalytic hydrogen peroxide production and flow-Fenton reaction, a new mechanism is proposed for the degradation process on Fe-CoSe-HT materials. Firstly, selenium-vacancy-enriched Fe-CoSe-HT monolayers could effectively promote the 2e-ORR catalytic activities. Then, reductive Fe-CoSe-HT could promote the conversion of Fe^{3+} and Fe^{2+} during Fenton-like reaction, which then continuously promote the generation of $\bullet$OH radical and degradation process. Hence, the dual role of Fe-CoSe-HT greatly enhanced selectivity of 2e-ORR and accelerated Fe reduction. The productive $\bullet$OH radical accumulation can greatly ensure an efficient remediation of organic pollutants.

4. Conclusion

In summary, we fabricated an selenium-vacancy-enriched trace Fe doped Fe-CoSe-HT through hydrothermal and further annealing
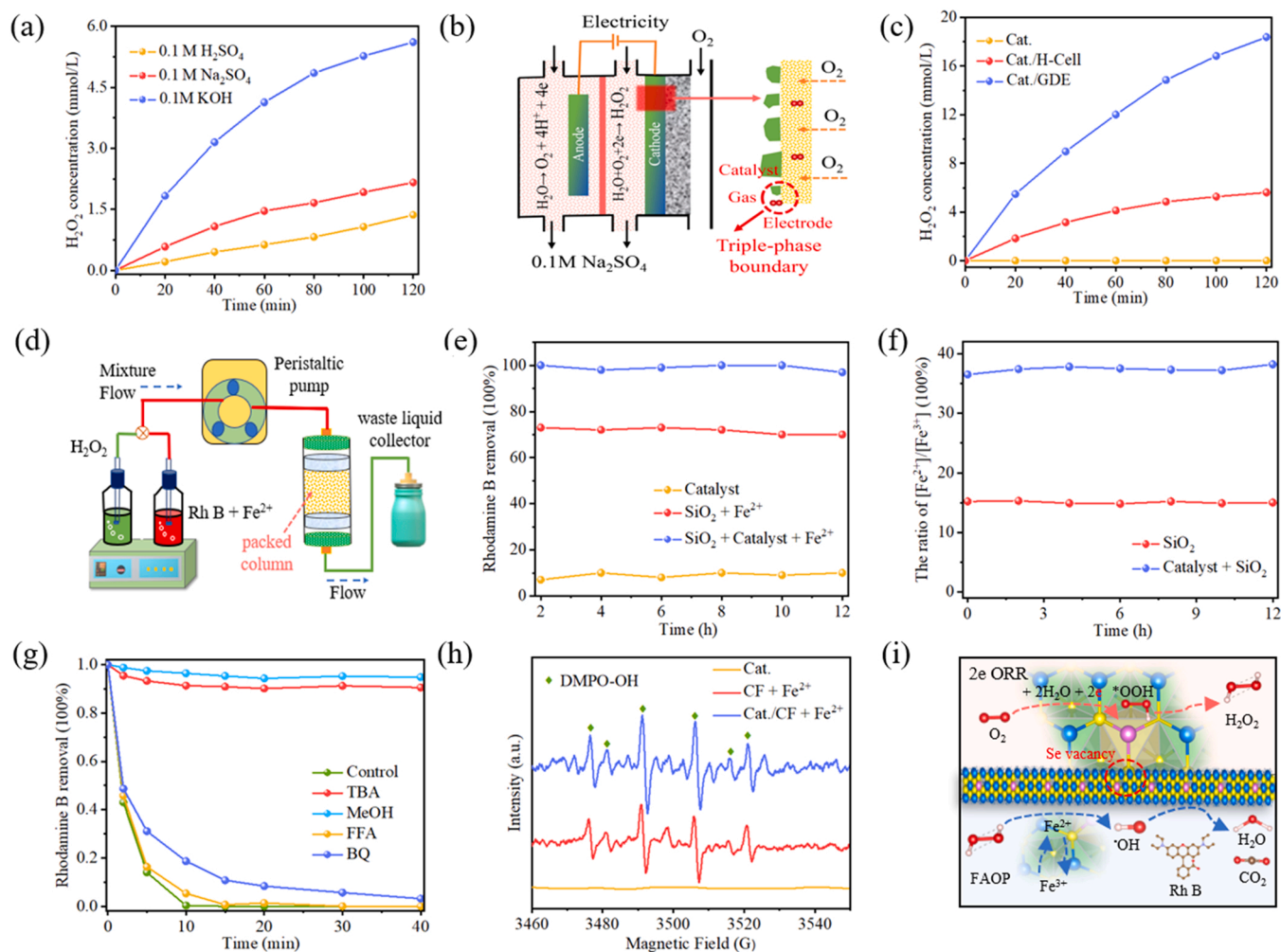
Fig. 5. (a) Profiles of H_2O_2 concentrations under alkaline, neutral and acidic conditions in traditional H-Cell electrode, (b) schematic diagram of flowing gas diffusion electrode (GDE) (c) contrast of H_2O_2 generation in traditional H-Cell and GDE devices, (d) coupling schematic diagram of electro-catalytic hydrogen peroxide production and flow Fenton-like reaction, (e) the degradation efficiency of Rhodamine B in catalyst packed column, (f) the ratio of Fe^{3+}/Fe^{2+} species, (g) radical quenching test, (h) EPR spectra of •OH radical, (i) the dual action of Fe-CoSe-HT material including selective electrosynthesis to hydrogen peroxides and built-in hydroxyl radical generation.

treatment. The introduction of teace Fe changes the crystal growth direction and induces the generation of Se vacancy during annealing. The results of XPS, HR-TEM, Raman spectra and microtherm EPR spectra prove the adequate Se-vacancy in synthetic Fe-CoSe-HT material. During rotating ring disk electrode measurements, the optimum Faradaic efficiency of synthetic Fe-CoSe-HT under 0.1 M KOH, 0.1 M Na_2SO_4 and 0.05 M H_2SO_4 can reach to 99.1%, 83.2% and 93.6%, respectively. Due to significantly improved tafel slope (432.4, 573.3 and 96.8 mV dec^{-1} in alkaline, neutral and acidic conditions) and highest ring current density in neutral (0.16 mA at 0.2 V), the concentration of H_2O_2 reached 18.37 mmol L^{-1} at 120 min when using GDE as the cathode in 0.1 M Na_2SO_4, almost 3.27 times than traditional H-Cell system. The enhanced reactivity stems from Fe introduction and the increased selenium vacancy in Fe-CoSe-HT atomic layers that optimizes the adsorption energy of the critical *OOH intermediates. Moreover, Fe-CoSe-HT exhibits good stability and versatile applicability the regeneration of Fe^{2+} in the flow-Fenton system. 100% RhB removal efficiency with outstanding stability is achieved in 12 h. Hence, the synthesized Fe-CoSe-HT materials greatly enhanced 2e-ORR selectivity and accelerated Fe reduction, which should facilitate the application of selenide in electrocatalysis and organic pollutants treatment.

CRediT authorship contribution statement

Jun Wang: Conceptualization, Methodology, Investigation, Writing – original draft. **Xiaomei Liu:** Formal analysis, Visualization. **Tao Liao:** Validation, Software. **Chengbo Ma:** Writing – review & editing. **Bin Chen:** Writing – review & editing. **Yang Li:** Writing – review & editing. **Xiaobin Fan:** Writing – review & editing. **Wenchao Peng:** Resources, Conceptualization, Writing – review & editing, Supervision, Data curation.

Declaration of Competing Interest

The authors declare that they have no known competing financial interests or personal relationships that could have appeared to influence the work reported in this paper.

Data Availability

Data will be made available on request.

Appendix A. Supporting information

Supplementary data associated with this article can be found in the online version at doi:10.1016/j.apcatb.2023.123344.

References

[1] C.B. Wu, Z.Y. Teng, C. Yang, F.S. Chen, H. Bin Yang, L. Wang, H.X. Xu, B. Liu, G. F. Zheng, Q. Han, Polarization engineering of covalent triazine frameworks for highly efficient photosynthesis of hydrogen peroxide from molecular oxygen and water, Adv. Mater. 34 (2022), 2110266.

[2] Y.Y. Sun, L. Silvioli, N.R. Sahraie, W. Ju, J.K. Li, A. Zitolo, S. Li, A. Bagger, L. Arnarson, X.L. Wang, T. Moeller, D. Bernsmeier, J. Rossmeisl, F. Jaouen, P. Strasser, Activity-selectivity trends in the electrochemical production of hydrogen peroxide over single-site metal-nitrogen-carbon catalysts, J. Am. Chem. Soc. 141 (2019) 12372–12381.

[3] Z. Zhou, Y. Kong, H. Tan, Q.W. Huang, C. Wang, Z.X. Pei, H.Z. Wang, Y.Y. Liu, Y. H. Wang, S. Li, X.Z. Liao, W.S. Yan, S.L. Zhao, Cation-Vacancy-enriched nickel phosphide for efficient electrosynthesis of hydrogen peroxides, Adv. Mater. 34 (2022), 2106541.

[4] J.M. Zhang, J. Ma, T.S. Choksi, D.J. Zhou, S.B. Han, Y.F. Liao, H.B. Yang, D. Liu, Z. P. Zeng, W. Liu, X.M. Sun, T.Y. Zhang, B. Liu, Strong metal-support interaction boosts activity, selectivity, and stability in electrosynthesis of H₂O₂, J. Am. Chem. Soc. 144 (2022) 2255–2263.

[5] H.N. Che, X. Gao, J. Chen, J. Hou, Y.H. Ao, P.F. Wang, Iodide-induced fragmentation of polymerized hydrophilic carbon nitride for high-performance quasi-homogeneous photocatalytic H₂O₂ production, Angew. Chem. Int. Ed. 60 (2021) 25546–25550.

[6] F. Wu, C. Pan, C.T. He, Y.H. Han, W.J. Ma, H. Wei, W.L. Ji, W.X. Chen, J.J. Mao, P. Yu, D.S. Wang, L.Q. Mao, Y.D. Li, Single-atom Co-N₄ electrocatalyst enabling four-electron oxygen reduction with enhanced hydrogen peroxide tolerance for selective sensing, J. Am. Chem. Soc. 142 (2020) 16861–16867.

[7] M.L. Pegis, C.F. Wise, D.J. Martin, J.M. Mayer, Oxygen reduction by homogeneous molecular catalysts and electrocatalysts, Chem. Rev. 118 (2018) 2340–2391.

[8] J.S. Adams, M.L. Kromer, J. Rodriguez-Lopez, D.W. Flaherty, Unifying concepts in electro- and thermocatalysis toward hydrogen peroxide production, J. Am. Chem. Soc. 143 (2021) 7940–7957.

[9] J.H. Kim, D. Shin, J. Lee, D.S. Baek, T.J. Shin, Y.T. Kim, H.Y. Jeong, J.H. Kwak, H. Kim, S.H. Joo, A general strategy to atomically dispersed precious metal catalysts for unravelling their catalytic trends for oxygen reduction reaction, ACS Nano 14 (2020) 1990–2001.

[10] Y. Gu, B.J.J. Xi, H. Zhang, Y.C.C. Ma, S.L.L. Xiong, Activation of main-group antimony atomic sites for oxygen reduction Catalysis, Angew. Chem. Int. Ed. 61 (2022), e202202200.

[11] J.J. Gao, H.B. Yang, X. Huang, S.F. Hung, W.Z. Cai, C.M. Jia, S. Miao, H.M. Chen, X.F. Yang, Y.Q. Huang, T. Zhang, B. Liu, Enabling direct H2O2 production in acidic media through rational design of transition metal single atom catalyst, Chem 6 (2020) 658–674.

[12] L. Fan, X.W. Bai, C. Xia, X. Zhang, X.H. Zhao, Y. Xia, Z.Y. Wu, Y.Y. Lu, Y.Y. Liu, H. T. Wang, CO₂/carbonate-mediated electrochemical water oxidation to hydrogen peroxide, Nat. Commun. 13 (2022) 2668.

[13] Q.R. Zhang, X. Tan, N.M. Bedford, Z.J. Han, L. Thomsen, S. Smith, R. Amal, X. Y. Lu, Direct insights into the role of epoxy groups on cobalt sites for acidic H₂O₂ production, Nat. Commun. 11 (2020) 4181.

[14] L.H. Yu, L. Tang, W. Guo, C.H. Li, D. Shin, Z.G. Liu, Y.M. Lin, Article Disclosing the natures of carbon edges with gradient nanocarbons for electrochemical hydrogen peroxide production, Matter 5 (2022) 1909–1923.

[15] H. Wang, W. Wang, H. Yu, Q. Mao, Y. Xu, X. Li, Z. Wang, L. Wang, Interface engineering of polyaniline-functionalized porous Pd metallene for alkaline oxygen reduction reaction, Appl. Catal. B: Environ. 307 (2022), 121172.

[16] Y.J. Chen, R. Gao, S.F. Ji, H.J. Li, K. Tang, P. Jiang, H.B. Hu, Z.D. Zhang, H.G. Hao, Q.Y. Qu, X. Liang, W.X. Chen, J.C. Dong, D.S. Wang, Y.D. Li, Atomic-level modulation of electronic density at cobalt single-atom sites derived from metal-organic frameworks: enhanced oxygen reduction performance, Angew. Chem. Int. Ed. 60 (2021) 3212–3221.

[17] X.F. Zhu, X. Tan, K.H. Wu, S.C. Haw, C.W. Pao, B.J. Su, J.J. Jiang, S.C. Smith, J. M. Chen, R. Amal, X.Y. Lu, Intrinsic ORR activity enhancement of pt atomic sites by engineering the d-band center via local coordination tuning, Angew. Chem. Int. Ed. 60 (2021) 21911–21917.

[18] M.M. Fan, Z.M. Wang, K. Sun, A. Wang, Y.Y. Zhao, Q.X. Yuan, R.B. Wang, J. Raj, J. J. Wu, J.C. Jiang, L. Wang, N-B-OH site-activated graphene quantum dots for boosting electrochemical hydrogen peroxide production, Adv. Mater. 35 (2023), 202209086.

[19] Y.L. Wang, G.I.N. Waterhouse, L. Shang, T.R. Zhang, Electrocatalytic oxygen reduction to hydrogen peroxide: from homogenous to heterogenous electrocatalysis, Adv. Energy Mater. 11 (2021), 202003323.

[20] M.M. Fan, Z.M. Wang, K. Sun, A. Wang, Y.Y. Zhao, Q.X. Yuan, R.B. Wang, J. Raj, J. J. Wu, J.C. Jiang, L. Wang, N-B-OH site-activated graphene quantum dots for boosting electrochemical hydrogen peroxide production, Adv. Mater. 35 (2023), 2209086.

[21] J.S. Lim, J.H. Kim, J. Woo, D. Baek, K. Ihm, T.J. Shin, Y.J. Sa, S.H. Joo, Designing highly active nanoporous carbon H₂O₂ production electrocatalysts through active site identification, Chem 7 (2021) 3114–3130.

[22] C. Zhang, W. Shen, K. Guo, M. Xiong, J. Zhang, X. Lu, A pentagonal defect-rich metal-free carbon electrocatalyst for boosting acidic O₂ reduction to H₂O₂ production, J. Am. Chem. Soc. 145 (2023) 11589–11598.

[23] Y.M. Wang, H. Huang, J. Wu, H.Y. Yang, Z.H. Kang, Y. Liu, Z.W. Wang, P. W. Menezes, Z.L. Chen, Charge-polarized selenium vacancy in nickel diselenide enabling efficient and stable electrocatalytic conversion of oxygen to hydrogen peroxide, Adv. Sci. 10 (2023), 202205347.

[24] L. An, Y. Hu, J.Y. Li, J.M. Zhu, M.Z. Sun, B.L. Huang, P.X. Xi, C.H. Yan, Tailoring oxygen reduction reaction pathway on spinel oxides via surficial geometrical-site occupation modification driven by the oxygen evolution reaction, Adv. Mater. 34 (2022), 202202874.

[25] Y.R. Zheng, S.J. Hu, X.L. Zhang, H.X. Ju, Z.B. Wang, P.J. Tan, R. Wu, F.Y. Gao, T. T. Zhuang, X. Zheng, J.F. Zhu, M.R. Gao, S.H. Yu, Black phosphorous mediates surface charge redistribution of CoSe₂ for electrochemical H₂O₂ production in acidic electrolytes, Adv. Mater. 34 (2022), 202205414.

[26] Z. Zhuang, A. Huang, X. Tan, K. Sun, C. Chen, Q. Peng, Z. Zhuang, T. Han, H. Xiao, Y. Zeng, W. Yan, J. Zhang, Y. Li, p-Block-metal bismuth-based electrocatalysts featuring tunable selectivity for high-performance oxygen reduction reaction, Joule 5 (2023) 1003–1015.

[27] C. Tang, L. Chen, H.J. Li, L.Q. Li, Y. Jiao, Y. Zheng, H.L. Xu, K. Davey, S.Z. Qiao, Tailoring acidic oxygen reduction selectivity on single-atom catalysts via modification of first and second coordination spheres, J. Am. Chem. Soc. 143 (2021) 7819–7827.

[28] R. Zhang, Y. Li, X. Zhou, A. Yu, Q. Huang, T. Xu, L. Zhu, P. Peng, S. Song, L. Echegoyen, F.F. Li, Single-atomic platinum on fullerene C₆₀ surfaces for accelerated alkaline hydrogen evolution, Nat. Commun. 14 (2023) 2460.

[29] C.Q. Zhang, L. Yuan, C. Liu, Z.M. Li, Y.Y. Zou, X.C. Zhang, Y. Zhang, Z.Q. Zhang, G. F. Wei, C.Z. Yu, Crystal engineering enables cobalt-based metal-organic frameworks as high-performance electrocatalysts for H₂O₂ production, J. Am. Chem. Soc. 145 (2023) 7791–7799.

[30] E. Jung, H. Shin, B.H. Lee, V. Efremov, S. Lee, H.S. Lee, J. Kim, W. Hooch Antink, S. Park, K.S. Lee, S.P. Cho, J.S. Yoo, Y.E. Sung, T. Hyeon, Atomic-level tuning of Co-N-C catalyst for high-performance electrochemical H₂O₂ production, Nat. Mater. 19 (2020) 436–442.

[31] H.Y. Sheng, A.N. Janes, R.D. Ross, D. Kaiman, J. Huang, B. Song, J.R. Schmidt, S. Jin, Stable and selective electrosynthesis of hydrogen peroxide and the electro-Fenton process on CoSe₂ polymorph catalysts, Energy Environ. Sci. 13 (2020) 4189–4203.

[32] R.D. Ross, H. Sheng, A. Parihar, J. Huang, S. Jin, Compositionally tuned trimetallic thiospinel catalysts for enhanced electrosynthesis of hydrogen peroxide and built-in hydroxyl radical generation, ACS Catal. 11 (2021) 12643–12650.

[33] X.L. Zhang, X.Z. Su, Y.R. Zheng, S.J. Hu, L. Shi, F.Y. Gao, P.P. Yang, Z.Z. Niu, Z. Z. Wu, S. Qin, R. Wu, Y. Duan, C. Gu, X.S. Zheng, J.F. Zhu, M.R. Gao, Strongly coupled cobalt diselenide monolayers for selective electrocatalytic oxygen reduction to H₂O₂ under acidic conditions, Angew. Chem. Int. Ed. 60 (2021) 26922–26931.

[34] K. Dong, J. Liang, Y.Y. Wang, Y.C. Ren, Z.Q. Xu, H.P. Zhou, L. Li, Q. Liu, Y.L. Luo, T.S. Li, A.M. Asiri, Q. Li, D.W. Ma, X.P. Sun, Plasma-induced defective TiO₂₋ₓ with oxygen vacancies: a high-active and robust bifunctional catalyst toward H₂O₂ electrosynthesis, Chem. Catal. 1 (2021) 1437–1448.

[35] L. Zhang, C.J. Lu, F. Ye, R.L.J. Pang, Y. Liu, Z.Y. Wu, Z.P. Shao, Z.M. Sun, L.F. Hu, Selenic Acid Etching Assisted Vacancy Engineering for Designing Highly Active Electrocatalysts toward the Oxygen Evolution Reaction, Adv. Mater. 33 (2021), 202007523.

[36] G.D. Fang, T. Zhang, H.B. Cui, D.D. Dionysiou, C. Liu, J. Gao, Y.J. Wang, D. M. Zhou, Synergy between Iron and Selenide on FeSe₂ (111) Surface Driving Peroxymonosulfate Activation for Efficient Degradation of Pollutants, Environ. Sci. Technol. 54 (2020) 15489–15498.

[37] Q. Zhong, C.M. Xu, Y.Z. Liu, Q.Y. Ji, Z. Xu, D.Y. Sun, S.H. Zhou, B. Yang, Y.H. Dai, C.D. Qi, S.G. Yang, H. He, S.Y. Li, C. Sun, Defect-engineered FeSe₂₋ₓ@C with porous architecture for enhanced peroxymonosulfate-based advanced oxidation processes, Appl. Catal. B: Environ. 309 (2022), 121259.

[38] B.J. Jing, S.J. You, Y.Y. Ma, Z.P. Xing, H. Chen, Y. Dai, C.Y. Zhang, N.Q. Ren, J. L. Zou, Fe₃Se₄/FeSe heterojunctions in cornstalk-derived N-doped carbon framework enhance charge transfer and cathodic oxygen reduction reaction to boost bio-electricity generation, Appl. Catal. B: Environ. 244 (2019) 465–474.

[39] J.W. Liu, S.H. Xiao, X.Y. Li, Z.Z. Li, X.R. Li, W.S. Zhang, Y. Xiang, X.B. Niu, J. S. Chen, Interface engineering of Fe₃Se₄/FeSe heterostructure encapsulated in electrospun carbon nanofibers for fast and robust sodium storage, Chem. Eng. J. 417 (2021), 141139.

[40] L.P. Wu, B. Li, Y. Li, X.B. Fan, F.B. Zhang, G.L. Zhang, Q. Xia, W.C. Peng, Preferential growth of the cobalt (200) facet in Co@N-C for Enhanced Performance in A Fenton-like Reaction, ACS Catal. 11 (2021) 5532–5543.

[41] Y. Jiang, M. Xie, F. Wu, Z.Q. Ye, Y.X. Zhang, Z.H. Wang, Y.Z. Zhou, L. Li, R.J. Chen, Cobalt selenide hollow polyhedron encapsulated in graphene for high-performance lithium/sodium storage, Small 17 (2021), 202102893.

[42] Y.H. Xie, J.Q. Cao, X.H. Wang, W.Y. Li, L.Y. Deng, S. Ma, H. Zhang, C. Guan, W. Huang, MOF-derived bifunctional Co₀.₈₅Se nanoparticles embedded in N-doped carbon nanosheet arrays as efficient sulfur hosts for lithium-sulfur batteries, Nano Lett. 21 (2021) 8579–8586.

[43] M.L. Li, C.Z. Shu, A.J. Hu, J.B. Li, R.X. Liang, J.P. Long, Invigorating the catalytic activity of cobalt selenide via structural phase transition engineering for lithium-oxygen batteries, ACS Sustain. Chem. Eng. 8 (2020) 5018–5027.

[44] J.L. Wang, K.P. Hou, Y.Z. Wen, H.L. Liu, H.L. Wang, K. Chakarawet, M. Gong, X. J. Yang, Interlayer structure manipulation of iron oxychloride by potassium cation intercalation to steer H_2O_2 activation pathway, J. Am. Chem. Soc. 144 (2022) 4294–4299.

[45] Y.Q. Zhao, B. Jin, Y. Zheng, H.Y. Jin, Y. Jiao, S.Z. Qiao, Charge state manipulation of cobalt selenide catalyst for overall seawater electrolysis, Adv. Energy Mater. 8 (2018), 201801926.

[46] Y.R. Zheng, P. Wu, M.R. Gao, X.L. Zhang, F.Y. Gao, H.X. Ju, R. Wu, Q. Gao, R. You, W.X. Huang, S.J. Liu, S.W. Hu, J.F. Zhu, Z.Y. Li, S.H. Yu, Doping-induced structural phase transition in cobalt diselenide enables enhanced hydrogen evolution catalysis, Nat. Commun. 9 (2018) 2533.

[47] H. Zhang, T.T. Wang, A. Sumboja, W.J. Zang, J.P. Xie, D.Q. Gao, S.J. Pennycook, Z. L. Liu, C. Guan, J. Wang, Integrated hierarchical carbon flake arrays with hollow p-doped CoSe2 nanoclusters as an advanced bifunctional catalyst for Zn-Air batteries, Adv. Funct. Mater. 28 (2018), 201804846.

[48] J.L. Liu, L.M. Zhang, H.J. Wu, Anion-doping-induced vacancy engineering of cobalt sulfoselenide for boosting electromagnetic wave absorption, Adv. Funct. Mater. 32 (2022), 202200544.

[49] M. Wang, Z. Sun, H. Ci, Z. Shi, L. Shen, C. Wei, Y. Ding, X. Yang, J. Sun, Identifying the evolution of selenium-vacancy-modulated $MoSe_2$ precatalyst in lithium–sulfur chemistry, Angew. Chem. Int. Ed. 60 (2021) 24558–24565.

[50] J. Wu, Y.D. Han, Y.C. Bai, X.T. Wang, Y.J. Zhou, W.X. Zhu, T.W. He, Y.M. Wang, H. Huang, Y. Liu, Z.H. Kang, The electron transport regulation in carbon dots/ In_2O_3 electrocatalyst enable 100% selectivity for oxygen reduction to hydrogen peroxide, Adv. Funct. Mater. 32 (2022), 202203647.

[51] C.Q. Zhang, R.H. Lu, C. Liu, J.Y. Lu, Y.Y. Zou, L. Yuan, J. Wang, G.Z. Wang, Y. Zhao, C.Z. Yu, Trimetallic sulfide hollow superstructures with engineered d-band center for oxygen reduction to hydrogen peroxide in alkaline solution, Adv. Sci. 9 (2022), 202104768.

[52] J.T. Ding, T. Fan, K. Shen, Y.W. Li, Electrochemical synthesis of amorphous metal hydroxide microarrays with rich defects from MOFs for efficient electrocatalytic water oxidation, Appl. Catal. B: Environ. 292 (2021), 120174.

[53] Z.P. Luo, M.T. Liu, D.Y. Tang, Y. Xu, H.H. Ran, J. He, K. Chen, J. Sun, High H_2O_2 selectivity and enhanced Fe^{2+} regeneration toward an effective electro-Fenton process based on a self-doped porous biochar cathode, Appl. Catal. B: Environ. 315 (2022), 121523.

[54] J. Wang, B. Li, Y. Li, X.B. Fan, F.B. Zhang, G.L. Zhang, W.C. Peng, Facile synthesis of atomic Fe-N-C materials and dual roles investigation of $Fe-N_4$ sites in fenton-like reactions, Adv. Sci. 8 (2021), 202101824.